



| | |
|-------------------------------|--|
| Publication Year | 2019 |
| Acceptance in OA @INAF | 2021-02-17T15:01:24Z |
| Title | A Hot Saturn Orbiting an Oscillating Late Subgiant Discovered by TESS |
| Authors | Huber, Daniel; Chaplin, William J.; Chontos, Ashley; Kjeldsen, Hans; Christensen-Dalsgaard, Jørgen; et al. |
| DOI | 10.3847/1538-3881/ab1488 |
| Handle | http://hdl.handle.net/20.500.12386/30434 |
| Journal | THE ASTRONOMICAL JOURNAL |
| Number | 157 |



| | |
|-------------------------------|--|
| Publication Year | 2019 |
| Acceptance in OA @INAF | 2021-02-17T15:01:24Z |
| Title | A Hot Saturn Orbiting an Oscillating Late Subgiant Discovered by TESS |
| Authors | Huber, Daniel; Chaplin, William J.; Chontos, Ashley; Kjeldsen, Hans; Christensen-Dalsgaard, Jørgen; et al. |
| DOI | 10.3847/1538-3881/ab1488 |
| Handle | http://hdl.handle.net/20.500.12386/30434 |
| Journal | THE ASTRONOMICAL JOURNAL |
| Number | 157 |



A Hot Saturn Orbiting an Oscillating Late Subgiant Discovered by *TESS*

Daniel Huber¹, William J. Chaplin^{2,3}, Ashley Chontos^{1,76}, Hans Kjeldsen^{3,4}, Jørgen Christensen-Dalsgaard³, Timothy R. Bedding^{3,5}, Warrick Ball^{2,3}, Rafael Brahm^{6,7,8}, Nestor Espinoza⁹, Thomas Henning⁹, Andrés Jordán^{7,8}, Paula Sarkis⁹, Emil Knudstrup³, Simon Albrecht³, Frank Grundahl^{3,4}, Mads Fredslund Andersen³, Pere L. Pallé^{10,11}, Ian Crossfield¹², Benjamin Fulton¹³, Andrew W. Howard¹⁴, Howard T. Isaacson¹⁵, Lauren M. Weiss¹, Rasmus Handberg³, Mikkel N. Lund³, Aldo M. Serenelli^{16,17}, Jakob Rørsted Mosumgaard³, Amalie Stokholm³, Allyson Bieryla¹⁸, Lars A. Buchhave¹⁹, David W. Latham¹⁸, Samuel N. Quinn¹⁸, Eric Gaidos²⁰, Teruyuki Hirano^{1,21}, George R. Ricker¹², Roland K. Vanderspek¹², Sara Seager^{12,22,23}, Jon M. Jenkins²⁴, Joshua N. Winn²⁵, H. M. Antia²⁶, Thierry Appourchaux²⁷, Sarbani Basu²⁸, Keaton J. Bell^{3,29}, Othman Benomar³⁰, Alfio Bonanno³¹, Derek L. Buzasi³², Tiago L. Campante^{33,34}, Z. Çelik Orhan³⁵, Enrico Corsaro³¹, Margarida S. Cunha³³, Guy R. Davies^{2,3}, Sebastien Deheuvels³⁶, Samuel K. Grunblatt¹, Amir Hasanzadeh³⁷, Maria Pia Di Mauro³⁸, Rafael A. García^{39,40}, Patrick Gaulme^{3,29}, Léo Girardi⁴¹, Joyce A. Guzik⁴², Marc Hon⁴³, Chen Jiang⁴⁴, Thomas Kallinger⁴⁵, Steven D. Kawaler⁴⁶, James S. Kuszewicz^{3,29}, Yveline Lebreton^{47,48}, Tanda Li^{3,5}, Miles Lucas⁴⁶, Mia S. Lundkvist^{3,49}, Andrew W. Mann⁵⁰, Stéphane Mathis^{39,40}, Savita Mathur^{10,11}, Anwesh Mazumdar⁵¹, Travis S. Metcalfe^{29,52}, Andrea Miglio^{2,3}, Mário J. P. F. G. Monteiro^{33,34}, Benoit Mosser⁴⁷, Anthony Noll³⁶, Benard Nsamba^{33,34}, Jia Mian Joel Ong²⁸, S. Örtel³⁵, Filipe Pereira^{33,34}, Pritesh Ranadive⁵¹, Clara Régulo^{10,11}, Thaïse S. Rodrigues⁴¹, Ian W. Roxburgh⁵³, Victor Silva Aguirre³, Barry Smalley⁵⁴, Mathew Schofield^{2,3}, Sérgio G. Sousa³³, Keivan G. Stassun^{55,56}, Dennis Stello^{3,5,43}, Jamie Tayar^{1,77}, Timothy R. White⁵⁷, Kuldeep Verma³, Mathieu Vrad³³, M. Yıldız³⁵, David Baker⁵⁸, Michaël Bazot³⁰, Charles Beichmann⁵⁹, Christoph Bergmann⁶⁰, Lisa Bugnet^{39,40}, Bryson Cale⁶¹, Roberto Carlino⁶², Scott M. Cartwright⁶³, Jessie L. Christiansen⁵⁹, David R. Ciardi⁵⁹, Orlagh Creevey⁶⁴, Jason A. Dittmann¹⁸, Jose-Dias Do Nascimento, Jr.^{18,65}, Vincent Van Eylen²⁵, Gabor Fürész¹², Jonathan Gagné⁶⁶, Peter Gao¹⁵, Kosmas Gazeas⁶⁷, Frank Giddens⁶⁸, Oliver J. Hall^{2,3}, Saskia Hekker^{3,29}, Michael J. Ireland⁵⁷, Natasha Latouf⁶¹, Danny LeBrun⁶¹, Alan M. Levine¹², William Matzko⁶¹, Eva Natinsky⁵⁸, Emma Page⁵⁸, Peter Plavchan⁶¹, Masoud Mansouri-Samani⁶², Sean McCauliff⁷⁵, Susan E. Mullally⁶⁹, Brendan Orenstein⁵⁷, Aylin Garcia Soto²², Martin Paegert¹⁸, Jennifer L. van Saders¹, Chloe Schnaible⁵⁸, David R. Soderblom⁶⁹, Róbert Szabó^{70,71}, Angelle Tanner⁷², C. G. Tinney⁶⁰, Johanna Teske^{66,73,77}, Alexandra Thomas^{2,3}, Regner Trampedach^{3,52}, Duncan Wright⁷⁴, Thomas T. Yuan⁵⁸, and Farzaneh Zohrabi⁷²

¹ Institute for Astronomy, University of Hawai'i, 2680 Woodlawn Drive, Honolulu, HI 96822, USA; huberd@hawaii.edu

² School of Physics and Astronomy, University of Birmingham, Birmingham B15 2TT, UK

³ Stellar Astrophysics Centre (SAC), Department of Physics and Astronomy, Aarhus University, Ny Munkegade 120, DK-8000 Aarhus C, Denmark

⁴ Institute of Theoretical Physics and Astronomy, Vilnius University, Sauletekio av. 3, 10257 Vilnius, Lithuania

⁵ Sydney Institute for Astronomy (SIFA), School of Physics, University of Sydney, NSW 2006, Australia

⁶ Center of Astro-Engineering UC, Pontificia Universidad Católica de Chile, Av. Vicuña Mackenna 4860, 7820436 Macul, Santiago, Chile

⁷ Instituto de Astrofísica, Facultad de Física, Pontificia Universidad Católica de Chile, Chile

⁸ Millennium Institute of Astrophysics, Av. Vicuña Mackenna 4860, 7820436 Macul, Santiago, Chile

⁹ Max-Planck-Institut für Astronomie, Königstuhl 17, D-69117 Heidelberg, Germany

¹⁰ Instituto de Astrofísica de Canarias (IAC), E-38205 La Laguna, Tenerife, Spain

¹¹ Universidad de La Laguna (ULL), Departamento de Astrofísica, E-38206 La Laguna, Tenerife, Spain

¹² Department of Physics and Kavli Institute for Astrophysics and Space Research, Massachusetts Institute of Technology, 77 Massachusetts Avenue, Cambridge, MA 02139, USA

¹³ NASA Exoplanet Science Institute/Caltech-IPAC, Pasadena, CA 91125, USA

¹⁴ California Institute of Technology, Pasadena, CA 91125, USA

¹⁵ Department of Astronomy, UC Berkeley, Berkeley, CA 94720, USA

¹⁶ Institute of Space Sciences (ICE, CSIC) Campus UAB, Carrer de Can Magrans, s/n, E-08193, Barcelona, Spain

¹⁷ Institut d'Estudis Espacials de Catalunya (IEEC), C/Gran Capita, 2-4, E-08034, Barcelona, Spain

¹⁸ Center for Astrophysics, Harvard & Smithsonian, 60 Garden Street, Cambridge, MA 02138, USA

¹⁹ DTU Space, National Space Institute, Technical University of Denmark, Elektrovej 328, DK-2800 Kgs. Lyngby, Denmark

²⁰ Department of Earth Sciences, University of Hawaii at Mānoa, Honolulu, HI 96822, USA

²¹ Department of Earth and Planetary Sciences, Tokyo Institute of Technology, 2-12-1 Ookayama, Meguro-ku, Tokyo 152-8551, Japan

²² Department of Earth, Atmospheric, and Planetary Sciences, Massachusetts Institute of Technology, 77 Massachusetts Avenue, Cambridge, MA 02139, USA

²³ Department of Aeronautics and Astronautics, Massachusetts Institute of Technology, 77 Massachusetts Avenue, Cambridge, MA 02139, USA

²⁴ NASA Ames Research Center, Moffett Field, CA 94035, USA

²⁵ Department of Astrophysical Sciences, Princeton University, 4 Ivy Lane, Princeton, NJ 08544, USA

²⁶ Tata Institute of Fundamental Research, Mumbai, India

²⁷ Univ. Paris-Sud, Institut d'Astrophysique Spatiale, UMR 8617, CNRS, Bâtiment 121, F-91405 Orsay Cedex, France

²⁸ Department of Astronomy, Yale University, P.O. Box 208101, New Haven, CT 06520-8101, USA

²⁹ Max-Planck-Institut für Sonnensystemforschung, Justus-von-Liebig-Weg 3, D-37077, Göttingen, Germany

³⁰ Center for Space Science, New York University Abu Dhabi, UAE

³¹ INAF—Osservatorio Astrofisico di Catania, via S. Sofia 78, I-95123, Catania, Italy

³² Department of Chemistry & Physics, Florida Gulf Coast University, 10501 FGCU Boulevard S., Fort Myers, FL 33965, USA

³³ Instituto de Astrofísica e Ciências do Espaço, Universidade do Porto, CAUP, Rua das Estrelas, 4150-762 Porto, Portugal

³⁴ Departamento de Física e Astronomia, Faculdade de Ciências da Universidade do Porto, Rua do Campo Alegre, s/n, PT4169-007 Porto, Portugal

³⁵ Department of Astronomy and Space Sciences, Science Faculty, Ege University, 35100, Bornova, İzmir, Turkey

³⁶ IRAP, Université de Toulouse, CNRS, CNES, UPS, Toulouse, France

- ³⁷ Department of Physics, University of Zanjan, Zanjan, Iran
- ³⁸ INAF-IAPS, Istituto di Astrofisica e Planetologia Spaziali, Via del Fosso del Cavaliere 100, I-00133 Roma, Italy
- ³⁹ IRFU, CEA, Université Paris-Saclay, F-91191 Gif-sur-Yvette, France
- ⁴⁰ AIM, CEA, CNRS, Université Paris-Saclay, Université Paris Diderot, Sorbonne Paris Cité, F-91191 Gif-sur-Yvette, France
- ⁴¹ Osservatorio Astronomico di Padova—INAF, Vicolo dell'Osservatorio 5, I-35122 Padova, Italy
- ⁴² Los Alamos National Laboratory, XTD-NTA, MS T-082, Los Alamos, NM 87545, USA
- ⁴³ School of Physics, The University of New South Wales, Sydney NSW 2052, Australia
- ⁴⁴ School of Physics and Astronomy, Sun Yat-Sen University, Guangzhou, 510275, People's Republic of China
- ⁴⁵ Institute of Astrophysics, University of Vienna, A-1180 Vienna, Austria
- ⁴⁶ Department of Physics and Astronomy, Iowa State University, Ames, IA 50011, USA
- ⁴⁷ LESIA, CNRS, Université Pierre et Marie Curie, Université Denis, Diderot, Observatoire de Paris, F-92195 Meudon cedex, France
- ⁴⁸ Univ Rennes, CNRS, IPR (Institut de Physique de Rennes)—UMR 6251, F-35000 Rennes, France
- ⁴⁹ Zentrum für Astronomie der Universität Heidelberg, Landessternwarte, Königstuhl 12, D-69117 Heidelberg, Germany
- ⁵⁰ Department of Physics and Astronomy, University of North Carolina at Chapel Hill, Chapel Hill, NC 27599, USA
- ⁵¹ Homi Bhabha Centre for Science Education, TIFR, V.N. Purav Marg, Mankhurd, Mumbai 400088, India
- ⁵² Space Science Institute, 4750 Walnut Street, Suite 205, Boulder, CO 80301, USA
- ⁵³ Astronomy Unit, Queen Mary University of London, Mile End Road, London, E1 4NS, UK
- ⁵⁴ Astrophysics Group, Lennard-Jones Laboratories, Keele University, Staffordshire ST5 5BG, UK
- ⁵⁵ Vanderbilt University, Department of Physics & Astronomy, 6301 Stevenson Center Lane, Nashville, TN 37235, USA
- ⁵⁶ Vanderbilt Initiative in Data-intensive Astrophysics (VIDA), 6301 Stevenson Center Lane, Nashville, TN 37235, USA
- ⁵⁷ Research School of Astronomy and Astrophysics, Australian National University, Canberra, ACT 2611, Australia
- ⁵⁸ Physics Department, Austin College, Sherman, TX 75090, USA
- ⁵⁹ Caltech/IPAC-NASA Exoplanet Science Institute, Pasadena, CA 91125, USA
- ⁶⁰ Exoplanetary Science at UNSW, School of Physics, UNSW Sydney, NSW 2052, Australia
- ⁶¹ Department of Physics and Astronomy, George Mason University 4400 University Avenue, Fairfax, VA 22030, USA
- ⁶² SGT Inc/NASA Ames Research Center, Moffett Field, CA 94035, USA
- ⁶³ Proto-Logic Consulting LLC, Washington, DC 20009, USA
- ⁶⁴ Université Côte d'Azur, Observatoire de la Côte d'Azur, CNRS, Laboratoire Lagrange, France
- ⁶⁵ Univ. Federal do Rio G. do Norte, UFRN, Dep. de Física, CP 1641, 59072-970, Natal, RN, Brazil
- ⁶⁶ Carnegie Institution of Washington DTM, 5241 Broad Branch Road NW, Washington, DC 20015, USA
- ⁶⁷ Section of Astrophysics, Astronomy and Mechanics, Faculty of Physics, National and Kapodistrian University of Athens, GR-15784 Zografos, Athens, Greece
- ⁶⁸ Missouri State University, USA
- ⁶⁹ Space Telescope Science Institute, 3700 San Martin Drive, Baltimore, MD 21212, USA
- ⁷⁰ MTA CSFK, Konkoly Observatory, Budapest, Konkoly Thege Miklós út 15-17, H-1121, Hungary
- ⁷¹ MTA CSFK Lendület Near-Field Cosmology Research Group
- ⁷² Mississippi State University, Department of Physics & Astronomy, Hilbun Hall, Starkville, MS 39762, USA
- ⁷³ Observatories of the Carnegie Institution for Science, 813 Santa Barbara Street, Pasadena, CA 91101, USA
- ⁷⁴ University of Southern Queensland, Toowoomba, Qld 4350, Australia

Received 2019 January 6; revised 2019 March 23; accepted 2019 March 26; published 2019 May 30

Abstract

We present the discovery of HD 221416 b, the first transiting planet identified by the *Transiting Exoplanet Survey Satellite* (*TESS*) for which asteroseismology of the host star is possible. HD 221416 b (HIP 116158, TOI-197) is a bright ($V = 8.2$ mag), spectroscopically classified subgiant that oscillates with an average frequency of about $430 \mu\text{Hz}$ and displays a clear signature of mixed modes. The oscillation amplitude confirms that the redder *TESS* bandpass compared to *Kepler* has a small effect on the oscillations, supporting the expected yield of thousands of solar-like oscillators with *TESS* 2 minute cadence observations. Asteroseismic modeling yields a robust determination of the host star radius ($R_\star = 2.943 \pm 0.064 R_\odot$), mass ($M_\star = 1.212 \pm 0.074 M_\odot$), and age (4.9 ± 1.1 Gyr), and demonstrates that it has just started ascending the red-giant branch. Combining asteroseismology with transit modeling and radial-velocity observations, we show that the planet is a “hot Saturn” ($R_p = 9.17 \pm 0.33 R_\oplus$) with an orbital period of ~ 14.3 days, irradiance of $F = 343 \pm 24 F_\oplus$, and moderate mass ($M_p = 60.5 \pm 5.7 M_\oplus$) and density ($\rho_p = 0.431 \pm 0.062 \text{ g cm}^{-3}$). The properties of HD 221416 b show that the host-star metallicity–planet mass correlation found in sub-Saturns ($4\text{--}8 R_\oplus$) does not extend to larger radii, indicating that planets in the transition between sub-Saturns and Jupiters follow a relatively narrow range of densities. With a density measured to $\sim 15\%$, HD 221416 b is one of the best characterized Saturn-size planets to date, augmenting the small number of known transiting planets around evolved stars and demonstrating the power of *TESS* to characterize exoplanets and their host stars using asteroseismology.

Key words: asteroseismology – techniques: photometric – planets and satellites: individual (HD 221416 b) – stars: fundamental parameters – planets and satellites: fundamental parameters

Supporting material: machine-readable table

⁷⁵ LinkedIn work performed at NASA Ames Research Center, Moffett Field, CA 94035, USA.

⁷⁶ NSF Graduate Research Fellow.

⁷⁷ Hubble Fellow.

1. Introduction

Asteroseismology is one of the major success stories of the space photometry revolution initiated by *CoRoT* (Baglin et al. 2006) and *Kepler* (Borucki et al. 2010). The detection of oscillations in thousands of stars has led to breakthroughs such as the discovery of rapidly rotating cores in subgiants and red giants, as well as the systematic measurement of stellar masses, radii, and ages (see Chaplin & Miglio 2013 for a review). Asteroseismology has also become the “gold standard” for calibrating more indirect methods to determine stellar parameters such as surface gravity ($\log g$) from spectroscopy (Petigura et al. 2017a) and stellar granulation (Mathur et al. 2011; Bastien et al. 2013; Kallinger et al. 2016; Corsaro et al. 2017; Bugnet et al. 2018; Pande et al. 2018), and age from rotation periods (gyrochronology; e.g., García et al. 2014; van Saders et al. 2016).

A remarkable synergy that emerged from space-based photometry is the systematic characterization of exoplanet host stars using asteroseismology. Following the first asteroseismic studies of exoplanet host stars using radial velocities (Bazot et al. 2005; Bouchy et al. 2005), the *Hubble Space Telescope* (Gilliland et al. 2011), and *CoRoT* (Ballot et al. 2011b; Lebreton & Goupil 2014), *Kepler* enabled the systematic characterization of exoplanets with over 100 detections of oscillations in host stars to date (Huber et al. 2013b; Lundkvist et al. 2016). In addition to the more precise characterization of exoplanet radii and masses (Ballard et al. 2014), the synergy also enabled systematic constraints on stellar spin-orbit alignments (Benomar et al. 2014; Chaplin et al. 2014a; Lund et al. 2014; Campante et al. 2016a) and statistical inferences on orbital eccentricities through constraints on the mean stellar density (Sliski & Kipping 2014; Van Eylen & Albrecht 2015; Van Eylen et al. 2019).

The recently launched NASA *Transiting Exoplanet Survey Satellite* (*TESS*) Mission (Ricker et al. 2014) is poised to continue the synergy between asteroseismology and exoplanet science. Using dedicated 2 minute cadence observations, *TESS* is expected to detect oscillations in thousands of main-sequence, subgiant, and early red-giant stars (Schofield et al. 2019), and simulations predict that at least 100 of these will host transiting or nontransiting exoplanets (Campante et al. 2016b). *TESS* host stars are on average significantly brighter than typical *Kepler* hosts, facilitating ground-based measurements of planet masses with precisely characterized exoplanet hosts from asteroseismology. While some of the first exoplanets discovered with *TESS* orbit stars that have evolved off the main sequence (Brahm et al. 2018; Nielsen et al. 2019; Wang et al. 2019), none of them were amenable to asteroseismology using *TESS* photometry. Here, we present the characterization of the HD 221416 (*TESS* Object of Interest 197, HIP 116158) system, the first discovery by *TESS* of a transiting exoplanet around a host star in which oscillations can be measured.

2. Observations

2.1. *TESS* Photometry

TESS observed HD 221416 in 2 minute cadence during Sector 2 of Cycle 1 for 27 days. We used the target pixel files produced by the *TESS* Science Processing Operations Center (Jenkins et al. 2016) as part of the *TESS* alerts on 2018 November 11.⁷⁸ We produced a light curve using the photometry pipeline⁷⁹

(R. Handberg et al. 2019, in preparation) maintained by the *TESS* Asteroseismic Science Operations Center (TASOC; Lund et al. 2017), which is based on software originally developed to generate light curves for data collected by the *K2* Mission (Lund et al. 2015).

Figure 1(a) shows the raw light curve obtained from the TASOC pipeline. The coverage is nearly continuous (duty cycle $\sim 93\%$), with a ~ 2 day gap separating the two spacecraft orbits in the observing sector. Two $\sim 0.1\%$ brightness dips, which triggered the identification of TOI-197.01 as a planet candidate, are evident near the beginning of each *TESS* orbit (see triangles in Figure 1(a)). The structure with a period of ~ 2.5 days corresponds to instrumental variations due to the angular momentum dumping cycle of the spacecraft.

To prepare the raw light curve for an asteroseismic analysis, the current TASOC pipeline implements a series of corrections as described by Handberg & Lund (2014), which includes the removal of instrumental artifacts and of the transit events using a combination of filters utilizing the estimated planetary period. Future TASOC-prepared light curves from full *TESS* data releases will use information from the ensemble of stars to remove common instrumental systematics (M. N. Lund et al. 2019, in preparation). Alternative light-curve corrections using transit removal and gap interpolation (García et al. 2011; Pires et al. 2015) yielded consistent results. The corrected TASOC light curve is shown in Figure 1(b). Figure 1(c) shows a power spectrum of this light curve, revealing the clear presence of a granulation background and a power excess from solar-like oscillations near $\sim 430 \mu\text{Hz}$, both characteristic of an evolved star near the base of the red-giant branch.

2.2. High-resolution Spectroscopy

We obtained high-resolution spectra of HD 221416 using several facilities within the *TESS* Follow-up Observation Program (TFOP), including HIRES (Vogt et al. 1994) on the 10 m telescope at Keck Observatory (Maunakea, Hawai’i); the Hertzprung SONG Telescope at Teide Observatory (Tenerife; Grundahl et al. 2017); HARPS (Mayor et al. 2003), FEROS (Kaufer et al. 1999), Coralie (Queloz et al. 2001), and FIDEOS (Vanzi et al. 2018) on the MPG/ESO 3.6 m, 2.2 m, 1.2 m, and 1 m telescopes at La Silla Observatory (Chile); Veloce (Gilbert et al. 2018) on the 3.9 m Anglo-Australian Telescope at Siding Spring Observatory (Australia); TRES (Fűrész 2008) on the 1.5 m Tillinghast reflector at the F. L. Whipple Observatory (Mt. Hopkins, Arizona); and iSHELL (Rayner et al. 2012) on the NASA IRTF Telescope (Maunakea, Hawai’i). All spectra used in this paper were obtained between 2018 November 11 and December 30 and have a minimum spectral resolution of $R \approx 44,000$. FEROS, Coralie, and HARPS data were processed and analyzed with the CERES package (Brahm et al. 2017a), which performs the optimal extraction and wavelength calibration of each spectrum, along with the measurement of precision radial velocities and bisector spans via the cross-correlation technique. Most instruments have been previously used to obtain precise radial velocities to confirm exoplanets, and we refer to the publications listed above for details on the reduction methods.

To obtain stellar parameters, we analyzed a HIRES spectrum using Specmatch (Petigura 2015), which has been extensively applied for the classification of *Kepler* exoplanet host stars (Johnson et al. 2017; Petigura et al. 2017a). The resulting parameters were $T_{\text{eff}} = 5080 \pm 70 \text{ K}$, $\log g = 3.60 \pm 0.08 \text{ dex}$, $[\text{Fe}/\text{H}] = -0.08 \pm 0.05 \text{ dex}$, and $v \sin i = 2.8 \pm 1.6 \text{ km s}^{-1}$,

⁷⁸ <https://doi.org/10.17909/t9-wx1n-aw08>

⁷⁹ <https://tasoc.dk/code/>

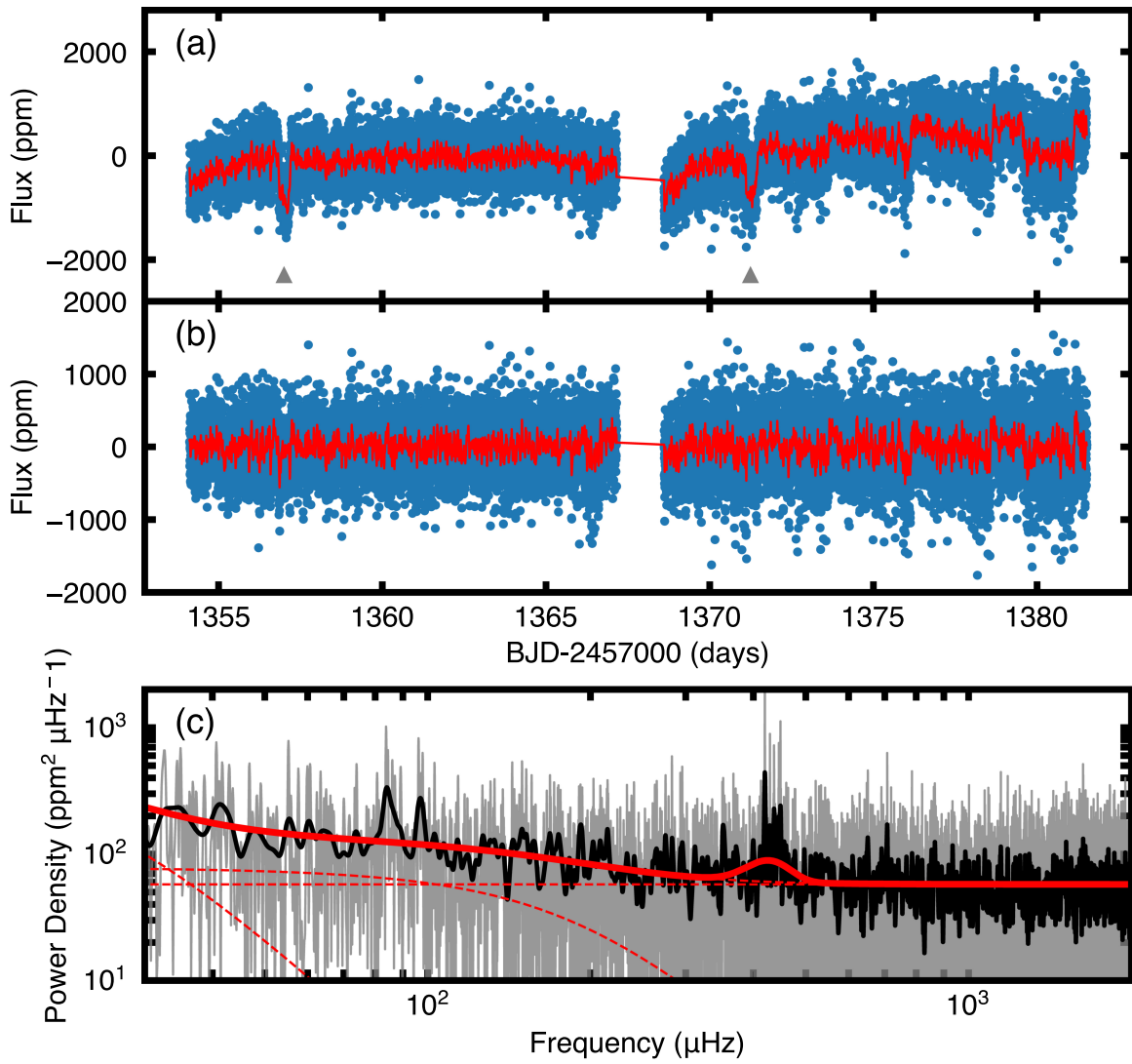


Figure 1. Panel (a): raw *TESS* 2 minute cadence light curve of HD 221416 produced by the *TESS* Asteroseismic Science Operations Center (TASOC). The red line is the light curve smoothed with a 10 minute boxcar filter (shown for illustration purposes only). Triangles mark the two transit events. Panel (b): light curve after applying corrections by the TASOC pipeline. Panel (c): power spectrum of panel (b), showing a granulation background and power excess due to oscillations near ~ 430 μHz . The solid red line is a global fit, consisting of granulation plus white noise and a Gaussian describing the power excess due to oscillations. Dashed red lines show the two granulation components and the white noise level, respectively.

consistent with an evolved star as identified from the power spectrum in Figure 1(c). To account for systematic differences between spectroscopic methods (Torres et al. 2012), we added 59 K in T_{eff} and 0.062 dex in $[\text{Fe}/\text{H}]$ in quadrature to the formal uncertainties, yielding final values of $T_{\text{eff}} = 5080 \pm 90$ K and $[\text{Fe}/\text{H}] = -0.08 \pm 0.08$ dex. Independent spectroscopic analyses yielded consistent results, including an analysis of a HIRES spectrum using ARES+MOOG (Sousa 2014; Sousa et al. 2018), FEROS spectra using ZASPE (Brahm et al. 2017b), TRES spectra using SPC (Buchhave et al. 2012) and iSHELL spectra using BT-Settl models (Allard et al. 2012).

2.3. Broadband Photometry and Gaia Parallax

We fitted the spectral energy distribution (SED) of HD 221416 using broadband photometry following the method described by Stassun & Torres (2016). We used NUV photometry from *GALEX*, $B_T V_T$ from *Tycho-2* (Høg et al. 2000), $B_V g_{ri}$ from APASS, JHK_S from 2MASS (Skrutskie et al. 2006), W1–W4 from *WISE* (Wright et al. 2010), and the G magnitude from *Gaia*

(Evans et al. 2018). The data were fit using Kurucz atmosphere models, with T_{eff} , $[\text{Fe}/\text{H}]$, and extinction (A_V) as free parameters. We restricted A_V to the maximum line-of-sight value from the dust maps of Schlegel et al. (1998). The resulting fit yielded $T_{\text{eff}} = 5090 \pm 85$ K, $[\text{Fe}/\text{H}] = -0.3 \pm 0.3$ dex, and $A_V = 0.09 \pm 0.02$ mag with a reduced χ^2 of 1.9, in good agreement with spectroscopy. Integrating the (dereddened) model SED gives the bolometric flux at Earth of $F_{\text{bol}} = (1.88 \pm 0.04) \times 10^{-8}$ erg s cm⁻². An independent SED fit using 2MASS, APASS9, USNO-B1, and *WISE* photometry and Kurucz models yielded excellent agreement, with $F_{\text{bol}} = (1.83 \pm 0.09) \times 10^{-8}$ erg s cm⁻² and $T_{\text{eff}} = 5150 \pm 130$ K. Additional independent analyses using the method by Mann et al. (2016) and PARAM (Rodrigues et al. 2014, 2017) yielded bolometric fluxes and extinction values that are consistent within 1σ with the values quoted above.

Combining the bolometric flux with the *Gaia* DR2 distance allows us to derive a nearly model-independent luminosity, which is a valuable constraint for asteroseismic modeling (see

Section 3.3). Using a *Gaia* parallax of 10.518 ± 0.080 mas (adjusted for the 0.082 ± 0.033 mas zero-point offset for nearby stars reported by Stassun & Torres 2018) with the two methods described above yielded $L_* = 5.30 \pm 0.14 L_\odot$ (using $F_{\text{bol}} = (1.88 \pm 0.04) \times 10^{-8} \text{ erg s cm}^{-2}$) and $L_* = 5.13 \pm 0.13 L_\odot$ (using $F_{\text{bol}} = (1.83 \pm 0.09) \times 10^{-8} \text{ erg s cm}^{-2}$). We also derived a luminosity using *isoclassify* (Huber et al. 2017),⁸⁰ adopting 2MASS *K*-band photometry, bolometric corrections from MIST isochrones (Choi et al. 2016), and the composite reddening map *mw dust* (Bovy et al. 2016), yielding $L_* = 5.03 \pm 0.13 L_\odot$. Our adopted luminosity was the mean of these methods with an uncertainty calculated by adding the mean uncertainty and scatter over all methods in quadrature, yielding $L_* = 5.15 \pm 0.17 L_\odot$.

2.4. High-resolution Imaging

HD 221416 was observed with the NIRC2 camera and Altair adaptive optics system on Keck II (Wizinowich et al. 2000) on UT 2018 November 25. Conditions were clear but seeing was poor ($0''.8$ – $2''$). We used the science target as the natural guide star, and images were obtained through a *K*-continuum plus KP50_{1.5} filter using the narrow camera (10 mas pixel scale). We obtained eight images (four each at two dither positions), each consisting of 50 coadds of 0.2 s each, with correlated double-sampling mode and four reads. Frames were coadded, and we subtracted an average dark image, constructed from a set of darks with the same integration time and sampling mode. Flat-fielding was performed using a dome flat obtained in the *K'* filter. “Hot” pixels were identified in the dark image and corrected by median filtering with a 5×5 box centered on each affected pixel in the science image. Only a single star appears in the images. We performed tests in which “clones” of the stellar image reduced by a specified contrast ratio were added to the original image. These show that we would have been able to detect companions as faint as $\Delta K = 5.8$ mag within $0''.4$ of HD 221416, 3.8 mag within $0''.2$, and 1.8 mag within $0''.1$.

Additional NIRC2 observations were obtained in the narrow-band Br γ filter ($\lambda_0 = 2.1686$; $\Delta\lambda = 0.0326 \mu\text{m}$) on UT 2018 November 22. A standard three-point dither pattern with a step size of $3''$ was repeated twice with each dither offset from the previous dither by $0''.5$. An integration time of 0.25 s was used with one coadd per frame for a total of 2.25 s on target, and the camera was used in the narrow-angle mode. No additional stellar companions were detected to within a resolution of $\sim 0''.05$ FWHM. The sensitivities of the final combined AO image were determined following Ciardi et al. (2015) and Furlan et al. (2017), with detection limits as faint as $\Delta\text{Br} - \gamma = 7.4$ mag within $0''.4$, 6.1 mag within $0''.2$, and 3.2 mag within $0''.1$.

The results from NIRC2 are consistent with Speckle observations using HRCam (Tokovinin et al. 2010) on the 4.1 m SOAR telescope.⁸¹ Because the companion is unlikely to be bluer than HD 221416, these constraints exclude any significant dilution (both for oscillation amplitudes and the depth of transit events).

3. Asteroseismology

3.1. Global Oscillation Parameters

To extract oscillation parameters characterizing the average properties of the power spectrum, we used several automated

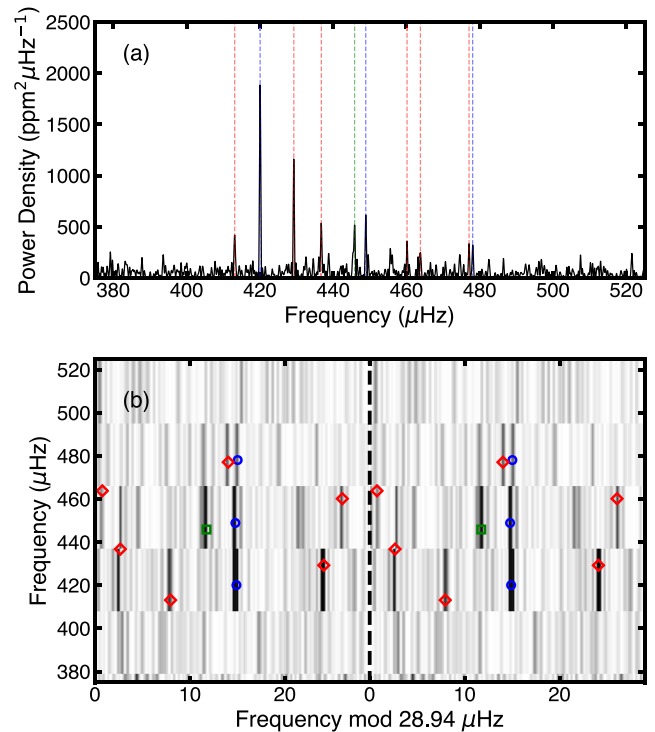


Figure 2. Panel (a): power spectrum of HD 221416 centered on the frequency region showing oscillations. Vertical dashed lines mark identified individual frequencies. Panel (b): grayscale échelle diagram (see footnote 83) of the background-corrected and smoothed power spectrum in panel (a). Identified individual mode frequencies are marked with blue circles ($l = 0$, radial modes), green squares ($l = 2$, quadrupole modes), and red diamonds ($l = 1$, dipole modes). Note that the diagram is replicated for clarity (Bedding 2012).

analysis methods (e.g., Huber et al. 2009; Mathur et al. 2010; Benomar et al. 2012; Kallinger et al. 2012; Mosser et al. 2012a; Corsaro & De Ridder 2014; Lundkvist 2015; Stello et al. 2017; Campante 2018; Bell et al. 2019), many of which have been extensively tested on *Kepler* data (e.g., Hekker et al. 2011; Verner et al. 2011). In most of these analyses, the power contributions due to granulation noise and stellar activity were modeled by a combination of power laws and a flat contribution due to shot noise, and then corrected by dividing the power spectrum by the background model. The individual contributions and background model using the method by Huber et al. (2009) are shown as dashed and solid red lines in Figure 1(c), and a close-up of the power excess is shown in Figure 2(a).

Next, the frequency of maximum power (ν_{max}) was measured either by heavily smoothing the power spectrum or by fitting a Gaussian function to the power excess. Our analysis yielded $\nu_{\text{max}} = 430 \pm 18 \mu\text{Hz}$, with uncertainties calculated from the scatter between all fitting techniques. Finally, the mean oscillation amplitude per radial mode was determined by taking the peak of the smoothed, background-corrected oscillation envelope and correcting for the contribution of nonradial modes (Kjeldsen et al. 2008a), yielding $A = 18.7 \pm 3.5$ ppm. We caution that the ν_{max} and amplitude estimates could be significantly biased by the stochastic nature of the oscillations. The modes are not well resolved, as demonstrated by the non-Gaussian appearance of the power spectrum and the particularly strong peak at $420 \mu\text{Hz}$.

Global seismic parameters such as ν_{max} and amplitude follow well-known scaling relations (Huber et al. 2011; Mosser et al. 2012b; Corsaro et al. 2013), allowing us to test whether

⁸⁰ <https://github.com/danxhuber/isoclassify>

⁸¹ <https://exofop.ipac.caltech.edu/tess/target.php?id=441462736>

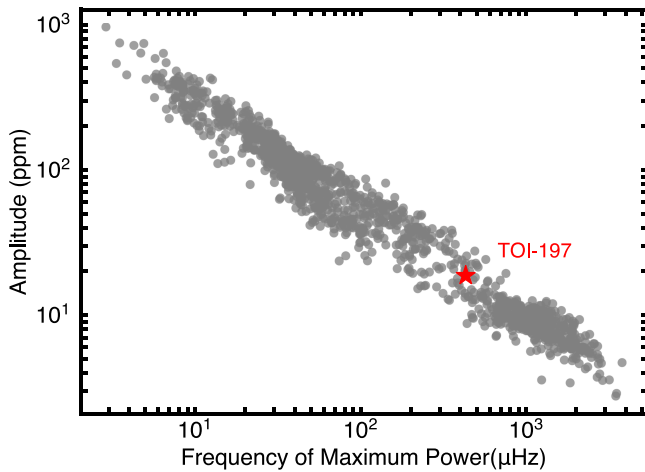


Figure 3. Amplitude per radial mode vs. frequency of maximum power for a sample of ~ 1500 stars spanning from the main sequence to the red-giant branch observed by *Kepler* (Huber et al. 2011). The red star shows the measured position of HD 221416 (TOI-197). The uncertainties are approximately equal to the symbol size.

the detected oscillations are consistent with expectations. Figure 3 compares our measured ν_{\max} and amplitude with results for ~ 1500 stars observed by *Kepler* (Huber et al. 2011). We observe excellent agreement, confirming that the detected signal is consistent with solar-like oscillations. We note that the oscillations in the *TESS* bandpass are expected to be $\sim 15\%$ smaller than in the bluer *Kepler* bandpass, which is well within the spread of amplitudes at a given ν_{\max} observed in the *Kepler* sample. The result confirms that the redder bandpass of *TESS* only has a small effect on the oscillation amplitude, supporting the expected rich yield of solar-like oscillators with *TESS* 2 minute cadence observations (Schofield et al. 2019).

3.2. Individual Mode Frequencies

The power spectrum in Figure 2(a) shows several clear peaks corresponding to individual oscillation modes. Given that *TESS* instrument artifacts are not yet well understood, we restricted our analysis to the frequency range 400–500 μHz where we observe peaks well above the background level.

To extract these individual mode frequencies, we used several independent methods ranging from traditional iterative sine-wave fitting, i.e., prewhitening (e.g., Kjeldsen et al. 2005; Lenz & Breger 2005; Bedding et al. 2007), to fitting of Lorentzian mode profiles (e.g., Handberg & Campante 2011; Appourchaux et al. 2012; Mosser et al. 2012b; Corsaro & De Ridder 2014; Corsaro et al. 2015; Vradar et al. 2015; Davies & Miglio 2016; Handberg et al. 2017; Roxburgh 2017; Kallinger et al. 2018), including publicly available code such as DIAMONDS.⁸² We required at least two independent methods to return the same frequency within uncertainties and that the posterior probability of each peak being a mode was $\geq 90\%$ (Basu & Chaplin 2017). A comparison of the frequencies returned by different fitters showed very good agreement, at a level smaller than the uncertainties for all reported modes. For the final list of frequencies, we adopted values from one fitter who applied prewhitening (HK), with uncertainties derived from Monte Carlo simulations of the data, as listed in Table 1.

Table 1

Extracted Oscillation Frequencies and Mode Identifications for HD 221416

| f (μHz) | σ_f (μHz) | l |
|------------------------|-------------------------------|-----|
| 413.12 | 0.29 | 1 |
| 420.06 | 0.11 | 0 |
| 429.26 | 0.14 | 1 |
| 436.77 | 0.24 | 1 |
| 445.85 | 0.21 | 2 |
| 448.89 | 0.21 | 0 |
| 460.16 | 0.33 | 1 |
| 463.81 | 0.43 | 1 |
| 477.08 | 0.31 | 1 |
| 478.07 | 0.35 | 0 |

Note. The large frequency separation derived from radial modes is $\Delta\nu = 28.94 \pm 0.15 \mu\text{Hz}$. Note that the $l = 1$ modes at ~ 460 and $\sim 463 \mu\text{Hz}$ are listed for completeness, but it is unlikely that both of them are genuine (see the text).

To measure the large frequency separation $\Delta\nu$, we performed a linear fit to all identified radial modes, yielding $\Delta\nu = 28.94 \pm 0.15 \mu\text{Hz}$. Figure 2(b) shows a grayscale échelle diagram⁸³ using this $\Delta\nu$ measurement, including the extracted mode frequencies. The $l = 1$ modes are strongly affected by mode bumping, as expected for the mixed-mode coupling factors for evolved stars in this evolutionary stage. The offset ϵ of the $l = 0$ ridge is ~ 1.5 , consistent with the expected value from *Kepler* measurements for stars with similar $\Delta\nu$ and T_{eff} (White et al. 2011).

3.3. Frequency Modeling

We used a number of independent approaches to model the observed oscillation frequencies, including different stellar evolution codes (ASTEC, Cesam2K, GARSTEC, Iben, MESA, and YREC; Iben 1965; Christensen-Dalsgaard 2008; Demarque et al. 2008; Morel & Lebreton 2008; Scuflaire et al. 2008; Weiss et al. 2008; Paxton et al. 2011, 2013, 2015; Choi et al. 2016), oscillation codes (ADIPLS, GYRE, and Pesnell; Pesnell 1990; Christensen-Dalsgaard 2008; Townsend & Teitler 2013), and modeling methods (including AMP, ASTFIT, BeSSP, BASTA, and PARAM; Deheuvels & Michel 2011; Lebreton & Goupil 2014; Rodrigues et al. 2014, 2017; Silva Aguirre et al. 2015; Yıldız et al. 2016; Ball & Gizon 2017; Creevey et al. 2017; Serenelli et al. 2017; Mosumgaard et al. 2018; Tayar & Pinsonneault 2018; Ong & Basu 2019). Most of the adopted methods applied corrections for the surface effect (Kjeldsen et al. 2008b; Ball & Gizon 2017). Model inputs included the spectroscopic temperature and metallicity, individual frequencies, $\Delta\nu$, and the luminosity (Section 2.3). To investigate the effects of different input parameters, modelers were asked to provide solutions using both individual frequencies and only using $\Delta\nu$, with and without taking into account the luminosity constraint. The constraint on ν_{\max} was not used in the modeling because it may be affected by finite mode lifetimes (see Section 3.1).

Overall, the modeling efforts yielded consistent results, and most modeling codes were able to provide adequate fits to the observed oscillation frequencies. The modeling confirmed that

⁸² <https://github.com/EnricoCorsaro/DIAMONDS>

⁸³ Échelle diagrams are constructed by dividing a power spectrum into equal segments with length $\Delta\nu$ and stacking one above the other, so that modes with a given spherical degree align vertically in ridges (Grec et al. 1983). Departures from regularity arise from sound speed discontinuities and from mixed modes, and thus probe the interior structure of a star.

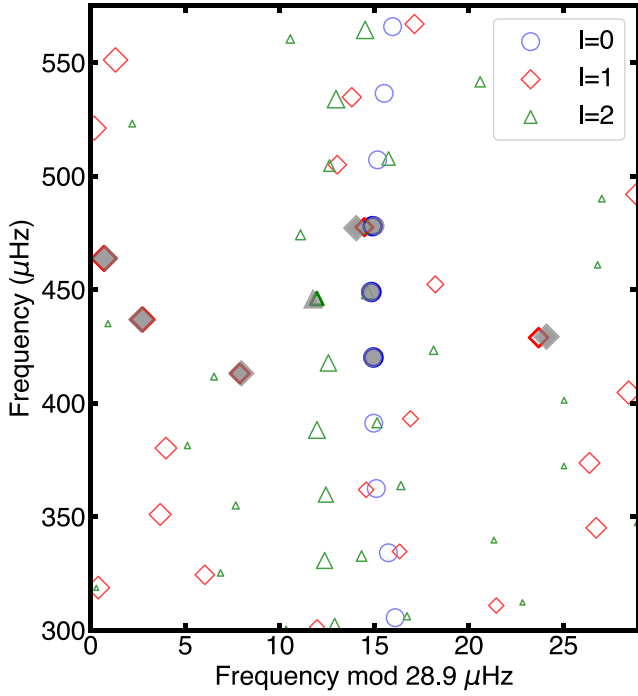


Figure 4. Échelle diagram showing observed oscillation frequencies (filled gray symbols) and a representative best-fitting model (open colored symbols) using GARSTEC, ADIPLS, and BeSSP (Serenelli et al. 2017). Model symbol sizes for nonradial modes are scaled using the mode inertia (a proxy for mode amplitude) as described in Cunha et al. (2015). Thick model symbols correspond to modes that were matched to observations. Uncertainties on the observed frequencies are smaller than or comparable to the symbol sizes. Note that the $l = 1$ mode at $460 \mu\text{Hz}$ has been omitted from this plot (see the text).

only one of the two closely spaced mixed modes near $\sim 460 \mu\text{Hz}$ is likely real, but we have retained both frequencies in Table 1 for consistency. An échelle diagram with observed frequencies and a representative best-fitting model is shown in Figure 4.

Independent analyses confirmed a bimodality splitting into lower mass, older models ($\sim 1.15 M_{\odot}$, ~ 6 Gyr), and higher mass, younger models ($\sim 1.3 M_{\odot}$, ~ 4 Gyr). Surface rotation would provide an independent mass diagnostic (e.g., van Saders & Pinsonneault 2013), but the insufficiently constrained $v \sin i$ and the unknown stellar inclination mean that we cannot decisively break this degeneracy. Combining an independent constraint of $\log g = 3.603 \pm 0.026$ dex from an autocorrelation analysis of the light curve (Kallinger et al. 2016) with a radius from L and T_{eff} favors a higher mass solution ($M_{\star} = 1.27 \pm 0.13 M_{\odot}$), but may be prone to small systematics in the ν_{max} scaling relation (which was used for the calibration). To make use of the most observational constraints available, we used the set of nine modeling solutions, which used T_{eff} , $[\text{Fe}/\text{H}]$, frequencies, and the luminosity as input parameters. From this set of solutions, we adopted the self-consistent set of stellar parameters with the mass closest to the median mass over all results. A more detailed study of the individual modeling results will be presented in a follow-up paper (T. Li et al. 2019, in preparation).

For ease of propagating stellar parameters to exoplanet modeling (see the next section), uncertainties were calculated by adding the median uncertainty for a given stellar parameter in quadrature to the standard deviation of the parameter for all methods. This method has been commonly adopted for

Table 2
Host Star Parameters

| Basic Properties | |
|---|-----------------------|
| HD ID | 221416 |
| Hipparcos ID | 116158 |
| TIC ID | 441462736 |
| V magnitude | 8.15 |
| $TESS$ magnitude | 7.30 |
| K magnitude | 6.04 |
| SED and <i>Gaia</i> Parallax | |
| Parallax, π (mas) | 10.518 ± 0.080 |
| Luminosity, L (L_{\odot}) | 5.15 ± 0.17 |
| Spectroscopy | |
| Effective temperature, T_{eff} (K) | 5080 ± 90 |
| Metallicity, $[\text{Fe}/\text{H}]$ (dex) | -0.08 ± 0.08 |
| Projected rotation speed, $v \sin i$ (km s^{-1}) | 2.8 ± 1.6 |
| Asteroseismology | |
| Stellar mass, M_{\star} (M_{\odot}) | 1.212 ± 0.074 |
| Stellar radius, R_{\star} (R_{\odot}) | 2.943 ± 0.064 |
| Stellar density, ρ_{\star} (gcc) | 0.06702 ± 0.00067 |
| Surface gravity, $\log g$ (cgs) | 3.584 ± 0.010 |
| Age, t (Gyr) | 4.9 ± 1.1 |

Note. The $TESS$ magnitude is adopted from the $TESS$ Input Catalog (Stassun et al. 2018).

Kepler (e.g., Chaplin et al. 2014b) and captures both random and systematic errors estimated from the spread among different methods. For completeness, the individual random and systematic error estimates are $R_{\star} = 2.943 \pm 0.041(\text{ran}) \pm 0.049(\text{sys}) R_{\odot}$, $M_{\star} = 1.212 \pm 0.052(\text{ran}) \pm 0.055(\text{sys}) M_{\odot}$, $\rho_{\star} = 0.06702 \pm 0.00019(\text{ran}) \pm 0.00047(\text{sys}) \text{gcc}$, and $t = 4.9 \pm 0.6(\text{ran}) \pm 0.9(\text{sys})$ Gyr. This demonstrates that systematic errors constitute a significant fraction of the error budget for all stellar properties (in particular stellar age), and emphasizes the need for using multiple model grids to derive realistic uncertainties for stars and exoplanets. The final estimates of the stellar parameters are summarized in Table 2, constraining the radius, mass, density, and age of HD 221416 to $\sim 2\%$, $\sim 6\%$, $\sim 1\%$ and $\sim 22\%$, respectively.

4. Planet Characterization

To fit the transits observed in the $TESS$ data, we used the PDC-MAP light curve provided by the $TESS$ Science Processing and Operations Center, which has been optimized to remove instrumental variability and preserve transits (Smith et al. 2012; Stumpe et al. 2014). To optimize computation time, we discarded all data more than 2.5 days before and after each of the two observed transits. We have repeated the fit and data preparation procedure using the TASOC light curve and found consistent results.

A total of 107 radial-velocity measurements from five different instruments (see Section 2.2 and Table 3) were used to constrain the mass of the planet. No spectroscopic observations were taken during transits, and hence the measurements are unaffected by the Rossiter–McLaughlin effect ($\sim 2.3 \text{ m s}^{-1}$ based on the measured $v \sin i$ and R_p/R_{\star}). To remove variations from stellar oscillations, we calculated weighted nightly means for all instruments that obtained multiple observations per night. We performed a joint

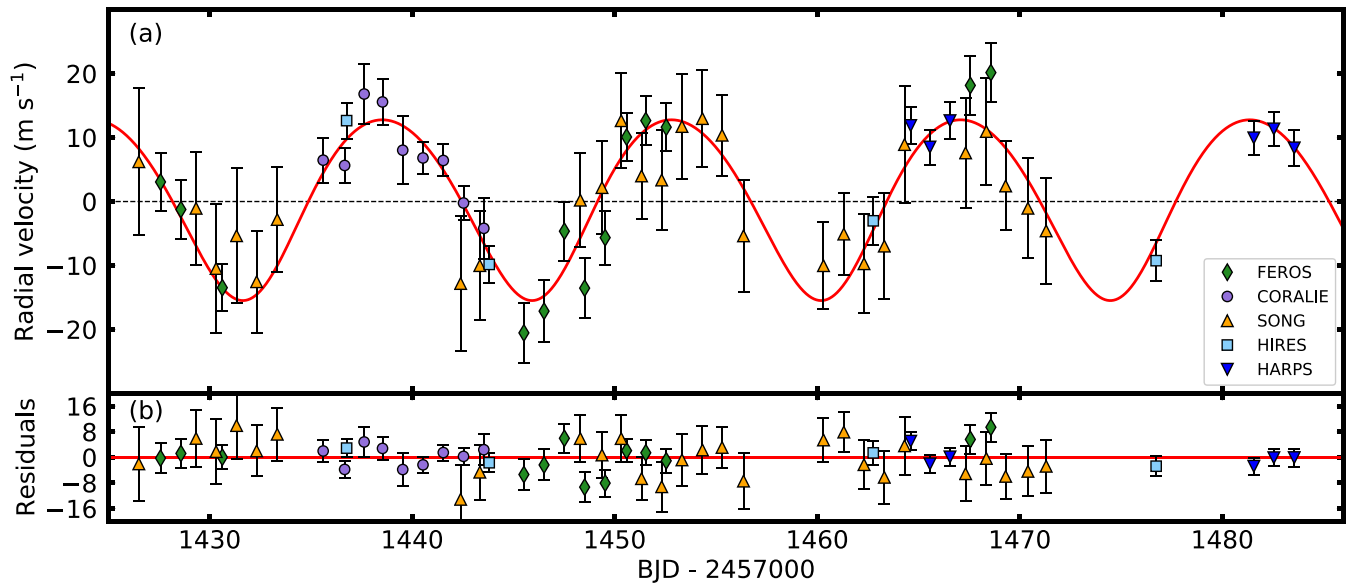


Figure 5. Radial-velocity time series (panel a) and residuals after subtracting the best-fitting model (panel b) for HD 221416 b. Data points are corrected for zero-point offsets of individual instruments, and error bars include contributions from stellar jitter.

Table 3
High-precision Radial Velocities for HD 221416

| Time (BJD) | RV (m s^{-1}) | σ_{RV} (m s^{-1}) | Instrument |
|----------------|--------------------------|--|------------|
| 2458426.334584 | 4.258 | 11.260 | SONG |
| 2458426.503655 | 6.328 | 11.270 | SONG |
| 2458427.575230 | -12.667 | 3.000 | FEROS |
| 2458428.547576 | 17.328 | 18.540 | SONG |
| ... | ... | ... | ... |
| 2458443.535340 | -14.667 | 3.600 | CORALIE |
| 2458443.541210 | -3.067 | 3.800 | CORALIE |
| 2458443.714865 | -6.815 | 0.780 | HIRES |
| 2458443.825283 | -4.375 | 0.720 | HIRES |
| ... | ... | ... | ... |
| 2458482.562290 | 19.433 | 2.000 | HARPS |
| 2458483.541710 | 16.133 | 2.000 | HARPS |
| 2458483.553240 | 19.233 | 2.000 | HARPS |
| 2458483.564690 | 16.233 | 2.000 | HARPS |

Note. Error bars do not include contributions from stellar jitter, and measurements have not been corrected for zero-point offsets.

(This table is available in its entirety in machine-readable form.)

transit and radial-velocity fit using a Markov Chain Monte Carlo algorithm based on the exoplanet modeling code *ktransit* (Barclay 2018), as described in Chontos et al. (2019). We placed a strong Gaussian prior on the mean stellar density using the value derived from asteroseismology (Table 2) and weak priors on the linear and quadratic limb-darkening coefficients, derived from the closest *I*-band grid points in Claret & Bloemen (2011), with a width of 0.6 for both coefficients. We also adopted a prior for the radial-velocity jitter from granulation and oscillations of $2.5 \pm 1.5 \text{ m s}^{-1}$, following Yu et al. (2018; see also Tayar et al. 2018), and a $1/e$ prior on the eccentricity to account for the linear bias introduced by sampling in $e \cos \omega$ and $e \sin \omega$ (Eastman et al. 2013). Independent zero-point offsets and stellar jitter values for each of the five instruments that provided radial velocities. Independent joint fits using EXOFASTv2 (Eastman et al. 2013) yielded consistent results.

Figures 5 and 6 show the radial-velocity time series, phase-folded transit and RV data, and the corresponding best-fitting model. Table 4 lists the summary statistics for all planet and model parameters. The system is well described by a planet in a 14.3 day orbit, which is nearly equal in size but $\sim 35\%$ less massive than Saturn ($R_p = 0.836 \pm 0.031 R_J$, $M_p = 0.190 \pm 0.018 M_J$), with tentative evidence for a mild eccentricity ($e = 0.11 \pm 0.03$). The long transit duration (~ 0.5 days) is consistent with a nongrazing ($b \approx 0.7$) transit given the asteroseismic mean stellar density, providing further confirmation for a gas-giant planet orbiting an evolved star. The radial-velocity data do not show evidence for any other short-period companions. Continued monitoring past the ~ 4 orbital periods covered here will further reveal details about the orbital architecture of this system.

5. Discussion

HD 221416 b joins an enigmatic but growing class of transiting planets orbiting stars that have significantly evolved off the main sequence. Figure 7 compares the position of HD 221416 within the expected population of solar-like oscillators to be detected with *TESS* (panel a) and within the known population of exoplanet host stars. Evolutionary states in Figure 7(b) have been assigned using solar-metallicity PARSEC evolutionary tracks (Bressan et al. 2012) as described in Berger et al. (2018).⁸⁴ HD 221416 sits at the boundary between subgiants and red giants, with the measured $\Delta\nu$ value indicating that the star has just started its ascent on the red-giant branch (Mosser et al. 2014). HD 221416 is a typical target for which we expect to detect solar-like oscillations with *TESS*, predominantly due to the increased oscillation amplitude, which are well known to scale with luminosity (Kjeldsen & Bedding 1995). On the contrary, HD 221416 is rare among known exoplanet hosts: while radial-velocity searches have uncovered a large number of planets orbiting red giants on long orbital periods (e.g., Wittenmyer et al. 2011), fewer than 15

⁸⁴ See also <https://github.com/danxhuber/evolstate>.

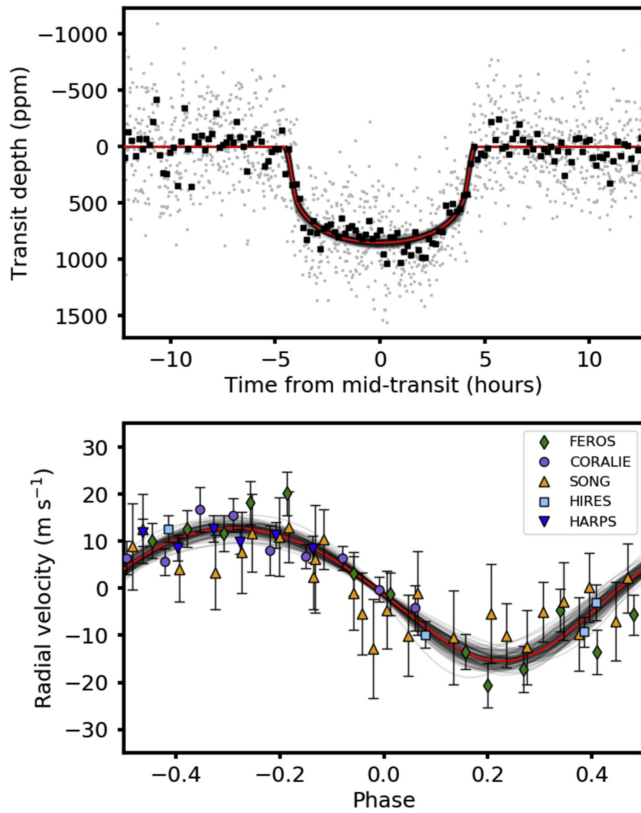


Figure 6. TESS light curve (panel a) and radial-velocity measurements (panel b) folded with the best-fitting orbital period. Gray points in panel (a) show the original sampling, and black points are binned means over 10 minutes. Red lines in both panels show the best-fitting model from the joint fit using stellar parameters, transit, and radial velocities. Gray lines show random draws from the joint MCMC model. Error bars in panel (b) include contributions from stellar jitter.

transiting planets are known around red-giant stars (as defined in Figure 7(b)). HD 221416 b is the sixth example of a transiting planet orbiting a late subgiant/early red giant with detected oscillations, following Kepler-91 (Barclay et al. 2013; Lillo-Box et al. 2014a, 2014b), Kepler-56 (Steffen et al. 2012; Huber et al. 2013a), Kepler-432 (Quinn et al. 2015; Ciceri et al. 2015), K2-97 (Grunblatt et al. 2016), and K2-132 (Grunblatt et al. 2017; Jones et al. 2018).

Transiting planets orbiting evolved stars are excellent systems to advance our understanding of the effects of stellar evolution on the structure and evolution of planets (see, e.g., Veras 2016 for a review). For example, such systems provide the possibility of testing the effects of stellar mass, evolution, and binarity on planet occurrence (e.g., Johnson et al. 2010; Schlaufman & Winn 2013; Stephan et al. 2018), which are still poorly understood. Furthermore, the increased irradiance on the planet caused by the evolution of the host star has been proposed as a means to distinguish between proposed mechanisms to explain the inflation of gas-giant planets beyond the limits expected from gravitational contraction and cooling (Hubbard et al. 2002; Lopez & Fortney 2016). Recent discoveries by the K2 mission have indeed yielded evidence that planets orbiting low-luminosity RGB stars are consistent with being inflated by the evolution of the host star (Grunblatt et al. 2016, 2017), favoring scenarios in which the energy from the star is deposited into the deep planetary interior (Bodenheimer et al. 2001).

Based on its radius and orbital period, HD 221416 b would nominally be classified as a warm Saturn, sitting between the

Table 4
Planet Parameters

| Parameter | Best Fit | Median | 84% | 16% |
|---------------------------|-----------|-----------|----------|----------|
| Model Parameters | | | | |
| γ_{HIRES} | 4.8 | 5.4 | +1.6 | -1.6 |
| γ_{SONG} | 1.1 | 0.2 | +1.5 | -1.5 |
| γ_{FEROS} | -15.4 | -15.7 | +1.2 | -1.2 |
| γ_{CORALIE} | -5.4 | -5.0 | +1.2 | -1.2 |
| γ_{HARPS} | 8.1 | 8.8 | +1.5 | -1.5 |
| σ_{HIRES} | 2.71 | 2.68 | +0.85 | -0.80 |
| σ_{SONG} | 2.06 | 2.11 | +0.91 | -0.89 |
| σ_{FEROS} | 3.49 | 3.47 | +0.75 | -0.71 |
| σ_{CORALIE} | 1.88 | 2.50 | +0.75 | -0.64 |
| σ_{HARPS} | 2.41 | 2.69 | +0.75 | -0.63 |
| z (ppm) | 199.4 | 199.1 | +10.6 | -10.7 |
| P (days) | 14.2762 | 14.2767 | +0.0037 | -0.0037 |
| T_0 (BTJD) | 1357.0135 | 1357.0149 | +0.0025 | -0.0026 |
| b | 0.744 | 0.728 | +0.040 | -0.049 |
| R_p/R_* | 0.02846 | 0.02854 | +0.00084 | -0.00071 |
| $e \cos \omega$ | -0.054 | -0.028 | +0.063 | -0.061 |
| $e \sin \omega$ | -0.099 | -0.096 | +0.029 | -0.030 |
| K (m s $^{-1}$) | 14.6 | 14.1 | +1.2 | -1.2 |
| ρ_* (gcc) | 0.06674 | 0.06702 | +0.00052 | -0.00052 |
| u_1 | 0.12 | 0.35 | +0.36 | -0.24 |
| u_2 | 0.71 | 0.44 | +0.30 | -0.44 |
| Derived Properties | | | | |
| e | 0.113 | 0.115 | +0.034 | -0.030 |
| ω | -118.7 | -106.0 | +34.7 | -31.1 |
| a (AU) | 0.1233 | 0.1228 | +0.0025 | -0.0026 |
| a/R_* | 9.00 | 8.97 | +0.27 | -0.27 |
| i ($^\circ$) | 85.67 | 85.75 | +0.36 | -0.35 |
| $R_p(R_\oplus)$ | 9.16 | 9.17 | +0.34 | -0.31 |
| $R_p(R_J)$ | 0.835 | 0.836 | +0.031 | -0.028 |
| $M_p(M_\oplus)$ | 63.4 | 60.5 | +5.7 | -5.7 |
| $M_p(M_J)$ | 0.200 | 0.190 | +0.018 | -0.018 |
| $\rho_p(\text{gcc})$ | 0.455 | 0.431 | +0.064 | -0.060 |

Note. Parameters denote velocity zero points γ , radial-velocity jitter σ , photometric zero-point z , orbital period P , time of transit T_0 , impact parameter b , star-to-planet radius ratio R_p/R_* , eccentricity e , argument of periastron ω , radial-velocity semi-amplitude K , mean stellar density ρ_* , linear and quadratic limb-darkening coefficients u_1 and u_2 , semimajor axis a , orbital inclination i , as well as planet radius (R_p), mass (M_p) and density (ρ_p).

well-known population of hot Jupiters and the ubiquitous population of sub-Neptunes uncovered by *Kepler* (Figure 8(a)). Taking into account the evolutionary state of the host star, however, HD 221416 b falls at the beginning of the “inflation sequence” in the radius–incident flux diagram (Figure 8(b)), with planet radius strongly increasing with stellar incident flux (Kovács et al. 2010; Demory & Seager 2011; Miller & Fortney 2011; Thorngren & Fortney 2018). Because HD 221416 b is currently not anomalously large compared to the observed trend and scatter for similar planets (Figure 8(b)) and low-mass planets are expected to be more susceptible to planet reinflation (Lopez & Fortney 2016), HD 221416 b may be a progenitor of a class of reinflated gas-giant planets orbiting RGB stars.

If confirmed, the mild eccentricity of HD 221416 b would be consistent with predictions of a population of planets around evolved stars for which orbital decay occurs faster than tidal circularization (Villaver et al. 2014; Grunblatt et al. 2018). Moreover, combining the asteroseismic age of the system with the possible nonzero eccentricity would allow constraints on the tidal